Journal of Materials Chemistry A

Accepted Manuscript

ROYAL SOCIETY OF CHEMISTRY

www.rsc.org/materialsA

Journal of Materials Chemistry A

Paper

Scalable Synthesis of Highly Dispersed Silicon Nanospheres by RF Thermal Plasma and Their Use as Anode Materials for High-Performance Li-ion Batteries

Received 00th January 20xx,
Accepted 00th January 20xx

DOI: 10.1039/x0xx00000x

www.rsc.org/

Guolin Hou[ab], Benli Cheng[c], Yuebin Cao[a], Mingshui Yao[d], Fei Ding[a], Peng Hu[a] and Fangli Yuan*[a]

Si nanospheres (SiNSs) have been synthesized via a simple, continuous and one-step way by using a radio frequency (RF) thermal plasma system in large-scale. Synthesized SiNSs display perfect spherical shape with smooth surface and good dispersity. By a simple ball-milling post-processing, silicon nanosphere/porous carbon (SiNS/PC) composites with synthesized Si nanospheres uniformly dispersed in the carbon matrix have been prepared, and the composite particles have a core/shell structure (i.e., every Si nanosphere is well covered by the complete porous carbon shell). As anodes for Li-ion batteries, the prepared composite materials could maintain microstructural stability after cycles and exhibit remarkably improved electrochemical performance with large storage capacity, super cycling stability and high rate capability. These desirable electrochemical performances are attributed to the unique structure of the SiNS/PC composite, which has a high capacity Si core with nanosphere morphology to alleviate the inner volume changes, and a porous shell acting as conductive matrix to enhance the conductivity, accommodate the silicon volume expansion, and facilitate lithium-ion transportation during charge-discharging.

1.Introduction

Lithium ion batteries (LIBs) are currently the dominant power sources for portable electronic devices, electric vehicles and grid-scale stationary energy storage.[1-4] Specially, high-performance LIBs are in urgent demand to address the ever-growing needs for improved energy density, owing to the rapid development of advanced electronic devices.[3,5-6] Considerable researches have been driven toward new electrode materials with high storage capacity and satisfactory cycle life such as Si,[7-9] Co_3O_4,[10-11] SnO_2,[12-14] Fe_3O_4[15-16] and NiO.[17-18] For anode materials, silicon stands out as the most promising material for the next generation LIBs due to its known highest theoretical capacity (4200 mA h g^{-1}),[19-20] which is almost ten times higher than that of graphite (372 mA h g^{-1}) currently used in commercial LIBs.[2,21-22] However, the practical application of silicon as anode material is seriously hindered by its low intrinsic electrical conductivity and the huge volume changes (>400%) during lithium insertion/extraction process, which cause the silicon particles dramatically pulverized and eventually lead to the capacity rapidly fading.[23-26]

To alleviate the volume changes and improve the overall electrochemical performance, various Si-based materials with different morphologies, structures and buffer matrixes, such as nanoparticles[7,22,27] (0D), nanowires[19,28-29], nanotubes[30] (1D), thin film[31] (2D) and Si/C nanocomposites[32-34] have been prepared. Among them, Si/C composites are regarded as effective structures to overcome the above drawbacks, as they could increase the electronic conductivity and alleviate the volume change at the same time. However, further improvement of electrochemical performance for Si/C composites is limited by the serious problem of the agglomeration of Si nanoparticles. The poor dispersion and agglomeration of Si nanoparticles in carbon lead to electrical disconnection and larger volume expansion during cyclings.[35] For example, Li et al. reported Si/C composite with using Si nanoparticles prepared by laser-induced silane gas reaction, which showed a reversible capacity of approximately 2900 mA h g^{-1} for the initial specific capacity. However, the capacity retention was less than 35% only after 10 cycles because of the serious agglomeration of Si nanoparticles in carbon.[25] Kwon also found that the volume expansion during cycling was greater than 300% even constantly increasing the amount of carbon black, in consequence of the difficulty in achieving homogeneous dispersion in carbon for non-uniform Si with aggregation.[36]

Recently, Cho and co-works demonstrated that nanosilicon with sphere morphology and smooth surface was apt to form homogeneous dispersion in carbon matrix due to its good

[a] State Key Laboratory of Multi-phase Complex Systems, Institute of Process Engineering, Chinese Academy of Sciences (CAS), Zhongguancun Beiertiao 1 Hao, Beijing 100190, P. R. China. E-mail: flyuan@home.ipe.ac.cn; Fax: +86-10-62561822; Tel: +86-10-82544974.
[b] University of Chinese Academy of Sciences (UCAS), No.19A Yuquan Road, Beijing 100049, P. R. China
[c] Green Eco-Manufacture Co.,Ltd. Tianjin Branch, Tianjin, 301600, P. R. China.
[d] State Key Laboratory of Structural Chemistry, Fujian Institute of Research on the Structure of Matter, Chinese Academy of Sciences (CAS), 155 Yangqiao Road west, Fuzhou, 350002, P. R. China.
† Electronic Supplementary Information (ESI) available: See DOI: 10.1039/x0xx00000x

particle mobility, and exhibited improved electrochemical performance.[22,37] For instance, Ng et al. reported carbon-coated Si nanocomposites produced by a spray-pyrolysis technique using dispersed Si nanosphere, which can reversibly store lithium with high capacity of 1489 mA h g^{-1} and stable coulombic efficiency above 99.5% even after 20 cycles.[34] Zhu et al. also found that the lithium storage performance of silicon was improved substantially by forming composite of nano-Si particles embedded homogeneously in graphene nanosheets (GNs) using plasma assisted milling (P-milling) method. The nano-Si/GNs composite exhibited enhanced cycling stability with a stable reversible capacity of 976 mA h g^{-1} at 50 mA g^{-1}, as the composite structure could inhibit the agglomeration of nano-Si and improve electronic conductivity.[38] However, at present, the realization of synthesis of Si nanospheres with high dispersion remains a challenging task. Si nanoparticles synthesized by solution synthesis,[39-40] thermal reduction[41] or decomposition[42-43] of silanes are usually result in serious agglomeration, which further leads to poor dispersion in carbon matrix and serious volume changes used as anode material for LIBs.

Herein, in this paper, we develop a facile scalable method for the synthesis of Si nanospheres (SiNSs) by using the radio-frequency induction thermal plasma (RF-plasma) system. The as-obtained particles present nearly perfect spherical shape and good dispersity. Specifically, by a simple ball-milling post processing, core/shell structure of silicon nanosphere/porous carbon (SiNS/PC) composite with Si nanospheres uniformly dispersed in the carbon matrix were synthesized. As anodes for LIBs, the obtained composites show significantly improved electrochemical performance with large capacity, high rate performance, and excellent cycling stability. These desirable property enhancements are attributed to the special SiNS/PC composite structure, which has a high capacity Si core with sphere morphology to alleviate the volume changes and a porous shell acting as conductive matrix to enhance the conductivity, accommodate the silicon volume expansion, and facilitate lithium-ion transportation during charge-discharging.

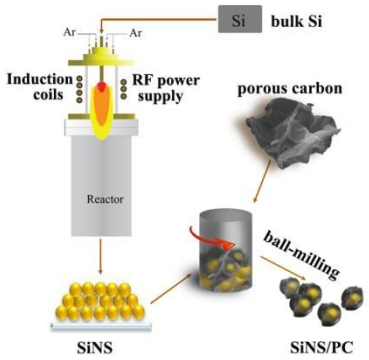

Scheme 1. The preparation process of SiNSs and SiNS/PC composites

2. Experimental sections

2.1 Materials synthesis

Synthesis of Si nanospheres

The material preparation process is shown in Scheme 1. Firstly, Si nanospheres were synthesized by using a radio frequency (RF) thermal plasma system in a one-step and continuous way. The experimental RF introduced plasma apparatus are composed of an RF generator (10 kW, 4 MHz), raw material feeder system, a quench/collection chamber, exhaust system and a gas supply and control system. Detail configuration of the apparatus is available in our published literature.[44] The starting powders of large size silicon (30-50 μm, irregular bulk), were delivered into the plasma flame by the carrier gas (Ar, 99.9%) in a continuous way. The evaporation reaction occurred in the plasma jet and was cooled down by the quenching gas, and products were obtained in the collection chamber. After reaction, yellowish-brown products in the collection chamber were harvested. The synthesis of nanoparticles by thermal plasma is an intricate heat and mass transfer process that involves phase conversion in a few tens of milliseconds, as well as interactions among the thermo fluid field, the induced electromagnetic field and the particle concentration field, all of which are described by numerous variables. Thus, the parameters for plasma processing are very important for stable operation and the typical operating parameters of plasma are given in Table S1 (Table S1, Supporting Information).

Synthesis of SiNS/PC nanocomposites

Secondly, the as-synthesized SiNSs were used to fabricate SiNS/PC nanocomposites by using a conventional planetary ball mill. A certain proportion of SiNSs mixed with porous carbon (Fig. S1, Supporting Information) were placed in a hard bearing steel vial under air atmosphere. The weight ratio of the steel ball to powder mixture was 10:1 and the rotation rate was 500 rpm min^{-1}. After the ball milling performing for 24 h, homogeneous SiNS/PC nanocomposites were obtained.

2.2 Materials characterization

The phase and crystal structure of obtained products were characterized by X-ray diffraction (XRD, Philips X' Pert PRO MPD) using the Cu Kα radiation operated at 40 kV and 30 mA. The morphologies of the products were observed by field-emission scanning electron microscope (FESEM, JSM-6700F, Tokyo, Japan). Detailed morphology and structure were characterized by transmission electron microscope (TEM, JEOL JEM-2100, Tokyo, Japan), high-resolution TEM (HRTEM) equipped with an energy-dispersive X-ray spectrometer (EDX). The porous property of the samples was investigated using physical adsorption of nitrogen at -196°C on a Brunauer–Emmett–Teller (BET) surface area analyzer (Micrometric, ASAP 2010). Raman spectroscopy (Renishaw, England) with an excitation wavelength of 514.5 nm was used to characterize the samples. The size distribution of the SiNS/PC composite before and after 50 cycles was measured and figured out by Nano-measurer program. Thermal gravimetric analyses (TGA) of SiNS/PC composite were performed with a TG-209 F3 instrument (NETZSCH, Germany) at a heating rate of 10°C min^{-1} under the nitrogen atmosphere.

2.3 Electrochemical measurements

CR2016 coin-type half-cell was assembled in an argon-filled glove box to test the electrochemical properties of SiNSs and SiNS/PC composites. The working electrode was prepared by mixing the active materials, acetylene black, and carboxymethylcellulose (CMC) binder in a weight ratio of 8:1:1 with deionized water as a solvent. Homogeneous slurry was obtained after the mixture being stirred for 45 min and was cast onto a common Cu foil (current collector). The film composed of Cu foil and slurries were dried at 80°C for 24 h and were cut into disks which were 14.0 mm in diameter, and then dried at 120°C under vacuum for 24 h. Lithium foils were used as the counter electrodes and polypropylene microporous films (Celgard 2400) as separators. The liquid electrolyte was 1 mol L^{-1} $LiPF_6$ in a mixture of ethylene carbonate (EC) and dimethyl carbonate (DMC) (1:1, v/v). The galvanostatic charge and discharge tests were conducted using the CT2001A LAND testing instrument (Wuhan LAND electronics Co., Ltd, China) in a voltage range between 0.01 and 1.5 V at the current density of 210, 420, 840, 2100 and 4200 mA g^{-1}. Cyclic voltammogram (CV) measurements were also carried out in the voltage range of 0.01-1.5 V at a scanning rate of 0.1 mV s^{-1} at room temperature.

3. Results and discussion

3.1. Characterization of SiNS

After treated by the thermal plasma, yellowish-brown, ultrafine Si powders were obtained in the collector. Information about the morphology and structure of as-synthesized products was characterized by FESEM and TEM. As shown in Fig. 1a, the nanoparticles with uniform size of about 50 nm show perfect spherical shape, smooth surface and good dispersity, and no particles with other shape or agglomeration are in sight from the FESEM images. Note that the specific surface area of synthesized products is measured to be 56.99 $m^2 g^{-1}$, which is consistent with the theoretical calculated value of spherical particles with a diameter of 46 nm. This result matches well with the size of SiNSs observed by SEM, further confirming that perfect nanospheres with a narrow size distribution were obtained. The detailed structural analyses of Si nanospheres were performed using TEM analysis in Fig. 1b, which clearly displays the uniform and smooth spherical shape. HRTEM (Fig. 1c) displays a clean and perfect crystalline structure and the measured lattice spacing of adjacent lattice planes is 0.31 nm, corresponding to (111) plane of Si crystal. All indicate that perfect single-crystalline Si nanospheres are obtained through RF thermal plasma processing.

An EDS spectroscopy (Fig. 1d) was conducted to measure the composition of as-prepared nanospheres (sample in Fig. 1a). It indicates that Si is the main element and very small O peak was detected in the EDS spectroscopy. XPS measurement was performed to further confirm the surface/near-surface chemical composition of Si nanospheres. As shown in Fig. 1e, it is mainly composed of Si, O and C elements according to the full-range XPS spectra, of which C contamination is mainly attributed to the residual solvents. More information about the chemical state of these elements can be obtained in the high resolution XPS spectra of the Si 2p and O 1s in Fig. 1f and g. The first peak at lower binding energy (BE, 98.7 eV) is assigned to the unoxidized Si atoms (Si^0) of the Si core, and the second peak at higher BE (103.1 eV) is attributed to fully oxidized Si (Si^{4+} states), in between is sub-oxidized Si components (Si^{x+} states), formed at the Si/SiO_2 interface.[45] In the O 1s spectra, the high BE component located at 532.5 eV is attributed to chemisorbed or dissociated oxygen on the surface of Si nanospheres, such as CO_2, O_2 or H_2O, while the typical BE (531 eV) of O^{2-} ions for SiO_2 is fair weak.[46-47] Therefore, the oxygen in the product is mainly derived from chemisorption and surface oxidation of Si nanospheres when exposed at ambient.

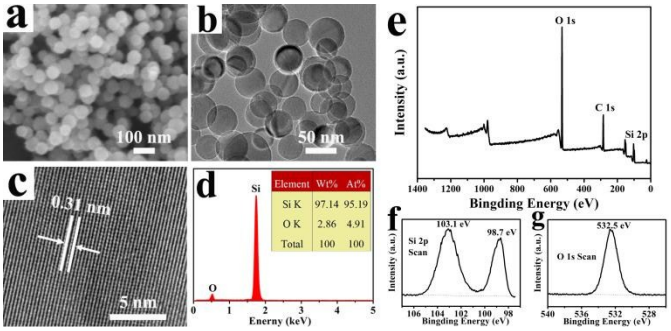

Fig. 1 (a) FESEM images, (b) TEM image, (c) lattice-resolved HRTEM image and (d) the EDS spectrum of as-prepared Si nanospheres. (e) XPS spectra and high resolution XPS spectra (f and g) of Si nanospheres at binding energies corresponding to Si 2p and O 1s.

3.2. Characterization of SiNS/PC composite

The as-synthesized SiNSs were used to fabricate the SiNS/PC nanocomposites by using a conventional planetary ball mill. As shown in Scheme 1, after the ball-milling performed for 24 h, homogeneous SiNS/PC nanocomposites were obtained. TG measurement was first carried out to estimate the Si contents in the SiNS/PC composites. Fig. 2 shows the TG curves of all samples in air. For PC, the weight loss located in 500-680°C is derived from carbon combustion, while pure SiNSs have a slight increased weight due to the partial oxidation in air atmosphere.[48] The sample of SiNS/PC composites with Si/C ratio of 0.5:1, 1:1 and 4:1 have a final retained weight of 32.7, 47.3 and 80.5 wt.%, respectively. These results match well with the Si content in the SiNS/PC composites with different Si/C ratios, confirming that SiNSs are uniformly dispersed in the carbon matrix.

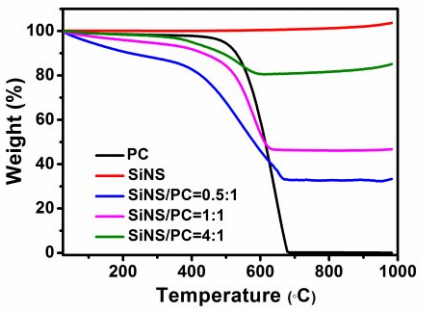

Fig. 2 TG curves under air atmosphere at the heating rate of 10°C min^{-1} of PC, SiNS and SiNS/PC composites with different Si/C ratios.

Fig. 3a shows the X-ray diffraction (XRD) patterns of the PC, SiNS and SiNS/PC composites with different Si/C ratios. Three diffraction peaks in the patterns of PC are agreement with the hexagonal phase of carbon (JCPDS No. 01-089-8487, space group: P63mc, lattice constants: a=b=2.4610 Å, c=6.7080 Å and α=β=90°, γ=120). The sharp diffraction peaks appeared at 28.4°, 47.3°, 56.1°, 69.1° and 76.4° in the XRD pattern of SiNS could be readily indexed to (111), (220), (311), (400), (331) and (422) planes of pure crystalline silicon (JCPDS No. 00-027-1402, space group: Fd-3m, lattice constants: a=b=c=5.431 Å, and α=β=γ=90°), respectively. For the XRD pattern of SiNS/PC composites, except for the typical diffraction peaks of Si, a weak diffraction peak of PC is also detected at 45° and slightly decreases with the increasing of Si/C ratio, indicating that SiNSs are highly dispersed in PC after ball milling. Note that the diffractions of Si and C of SiNS/PC composites show no shift or change, suggesting that the ball-milling process does not destroy the original structure of Si and C. Raman spectroscopy is widely used to obtain structural information about carbon-based materials. Thus, Raman measurement was performed to further confirm the chemical composition of SiNS/PC composite. As shown in Fig. 3b, the sharp peak at around 511 cm^{-1} is attributed to the crystalline nature of Si.[49] The characteristic peak at 1350 cm^{-1} is ascribed to the D band, corresponding to the amorphous carbon, while the peak at 1580 cm^{-1} is attributed to the G band, corresponding to the graphitic carbon.[50] Note that the two characteristic peaks of carbon slightly weaken with the decrease of C ratio in SiNS/PC composites, further indicating that SiNSs are highly dispersed in PC after ball milling.

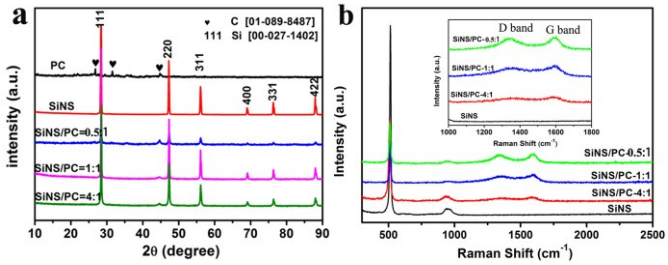

Fig. 3 (a) Typical XRD patterns and (b) Raman spectra of PC, SiNS and SiNS/PC composites with different Si/C ratios.

After ball milling process, all SiNS/PC composites represent similar structure, and with the increase of carbon contents, the carbon layers incrassate and become more uniform (Fig. S3, Supporting Information). Detailed morphology, structure and compose of the SiNS/PC-4:1 composite were characterized by FESEM and TEM. As shown in Fig. 4a, Si nanoparticles are uniformly dispersed in the carbon matrix and no Si agglomerates are in sight from the FESEM images. The TEM image in Fig. 4b reveals that all particles have core/shell structure and every nanoparticle is well covered in the complete shell. The thickness of this shell is around 5-20 nm, whereas the diameter of core is around 30-50 nm, which matches well with the size of pure SiNS. Close examination of an individual composite particle by TEM in Fig. 4c and d substantiate that the particle is composed of a clean and perfect crystalline structure core and an amorphous carbon shell with a thickness of about 5 nm. The measured lattice spacing of the internal core of 0.31 nm could be readily indexed to (111) plane of Si crystal, suggesting that ball milling process did not change the internal crystallite structure of SiNS. The elemental mapping images taken from Fig. 4c present a red ring of carbon elemental distribution (Fig. 4e) and a smaller size sphere of silicon elemental distribution (Fig. 4g), also indicating a perfect core-shell structure of the SiNS/PC composite. The thin yellow ring of O elemental distribution (Fig. 4f) is nearly equal to that of silicon elemental distribution and smaller than that of C elemental distribution, suggesting that the O element mainly distributes thinly on the surface of Si nanosphere. This result matches well with the HRTEM images of single Si nanosphere (Fig. S4, Supporting Information). The elemental mapping, together with the HRTEM result, confirms that well wrapped SiNS/PC composites were successfully synthesized. Such a structure should be very interesting for lithium storage as it has a high capacity Si core and a conductive porous shell to accommodate the silicon volume expansion during charging.

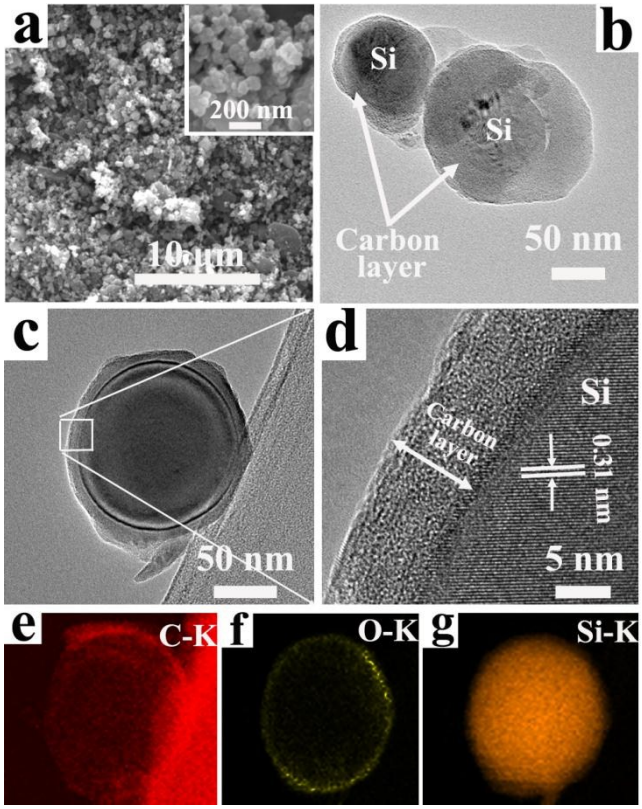

Fig. 4 (a) SEM image and (b) TEM image of as-prepared SiNS/PC-4:1, (c) TEM image, (d) lattice-resolved HRTEM image and (e-g) elemental mapping (C: red; O: yellow; Si: orange) of single SiNS/PC-4:1 particle.

It was found that a compact carbon coating on Si is usually ruptured upon volume expansion after cycles, exposing Si to electrolytes and leading to continual SEI deposition.[34] Thus, the SiNS/PC composites are expected to provide volume for

silicon expanding during charge-discharging by introducing "void". Brunauer–Emmett–Teller (BET) surface area and porosity were determined by Nitrogen adsorption–desorption measurement. As is shown in Fig. 5, the adsorption and desorption isotherms of SiNS/PC depict typical I type with isotherm bias toward Y axis at low relative pressure, indicating the presence of micropores.[51] The BET surface area calculated from the linear part of the BET plot is about 178.558 $m^2 g^{-1}$, which is about 3 times that of the SiNS. The corresponding pore size distribution curve calculated from the desorption branch by the Barett-Joyner-Halenda (BJH) method in the inset of Fig. 6 displays a pore size distribution of 1-5 nm, centered at 1 nm. It agrees well with the pore size distribution of raw material porous carbon (Fig. S2, Supporting Information), indicating that the original microporous structure of PC was not destroyed by the ball-milling process and kept in the shell of SiNS/PC.

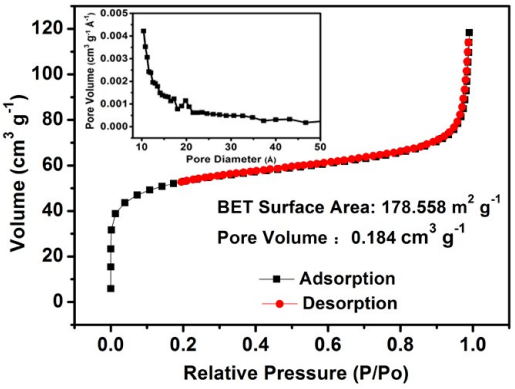

Fig. 5 N_2 adsorption–desorption isotherm of the SiNS/PC composite and the inset is the corresponding BJH pore size distribution.

3.3. Electrochemical performance of SiNS and SiNS/PC

CR2016 coin-type half-cells with a metallic lithium counter electrode were used to test the electrochemical performance of the SiNSs and the SiNS/PC composites. To investigate the intrinsic properties of the SiNSs, galvanostatic cycling was used with voltage cutoffs of 0.01 and 1.5 V vs Li/Li^+. Fig. 6a shows the charge and discharge curves of SiNS electrodes at a current density of 210 mA g^{-1}. For SiNS, the initial cycle discharge-charge curves show a broader discharge lithiation voltage plateau at about 0.05-0.1 V corresponding to the formation of Si-Li alloy by Li insertion, and a charge delithiation voltage plateau at about 0.35-0.45 V corresponding to the Li extraction.[52-53] Note that the first cycle discharge capacity of SiNS reaches to 2388 mA h g^{-1}, confirming that the as-synthesized SiNSs exhibit favorable advantage as high energy density materials for Si-based LIB anode. However, the SiNS electrode shows a low initial charge capacity of 1703 mA h g^{-1}, resulting in a low initial coulombic efficiency (ICE) of 71%. The lower ICE is ascribed to the formation of solid electrolyte interphase (SEI) on the surface of electrode, and the irreversible insertion of lithium ions into the Si particles.[54-55] The irreversible capacity phenomenon in the initial cycle of Si-based electrodes in lithium batteries is very common.[54,56-57]

Cyclic voltammetry (CV) was further conducted to characterize the electrochemical performance of the SiNS electrodes in a voltage range of 0.01-2.0 V (versus Li/Li^+) at a sweep rate of 0.1 mV s^{-1} shown in Fig. 6b. In the first discharge process, the broad cathodic peak appearing at around 0.78 V in the first cycle and disappearing in subsequent cycles is related to the formation of SEI layer, which matches well with the result of the initial charge and discharge curve of SiNS electrode. The two peaks at 0.01 and 0.16 V at the cathodic branch (Li alloy) of the CV curve are corresponding to the formation of Li_xSi alloy phases, while the two peaks at 0.35 and 0.52 V at the anodic branch (Li dealloy) could be ascribed to de-lithiation back to Si.[58-59] The data of the CV curve is well consistent with the results previously reported in the literature for Si electrodes.[20,56,60]

Cycling performance is an extremely important factor for lithium ion battery and directly determines its practical application. Fig. 6c shows the cycling performances of SiNS and SiIP (Si irregular particle) electrodes at the current density of 210 mA g^{-1}. In the first cycle, the discharge capacity of SiIP electrode is 1126 mA h g^{-1}, however, the SiIP electrode shows a low initial charge capacity of 501 mA h g^{-1}, resulting in a low initial coulombic efficiency (ICE) of only 45%. After 5 cycles, it rapidly decays to 22.5 mA h g^{-1}. The rapid capacity decay is ascribed to the microstructural pulverization and disruption of the electrode caused by silicon repeatedly expansion-contraction during the Li^+ insertion-extraction process, finally leading to the loss of electrical conductivity.[61-62] However, for SiNS electrode, the initial specific capacities was 2388 mA h g^{-1}, with an initial coulombic efficiency (ICE) of 71%. After 5 cycles, the coulombic efficiency stabilizes at 99.5% and the specific capacitie stabilizes at about 700 mA h g^{-1}. Importantly, after 50 cycles, the specific discharge capacity of SiNS electrode is still 500 mA h g^{-1}. The great capacity retention for the SiNS electrode could be attributed to the high dispersion and nanospherical structure of the SiNS, which could effectively reduce the volume changes during charge-discharging, and thus improving the capacity and cycling stability.

The electrochemical impedance spectroscopy (EIS) was used to further study the charge transfer and ion diffusion kinetics of the SiNS and SiIP electrodes. Their Nyquist plots determined in the frequency range of 0.01 Hz to 100 kHz, carried out at the lithiated state (10 mV vs Li/Li^+) at room temperature, are shown in Fig. 6d. The typical impedance spectrum is consisted of a semicircle assigned to the charge-transfer resistance at the electrode-electrolyte interface in the high frequency range, and a straight line implied the Li^+ diffusion-controlled processes in the solid electrode in the low frequency range.[59] Compared with SiIP electrode, the diameter of the semicircle for the SiNS electrode is much smaller, indicating lower charge-transfer resistance at the electrode/solution interface. This dramatic reduce of resistance could be attributed to the shortened lithium ion transmission path of SiNS electrode, which can effectively facilitate lithium-ion transportation during charge-discharging.[63]

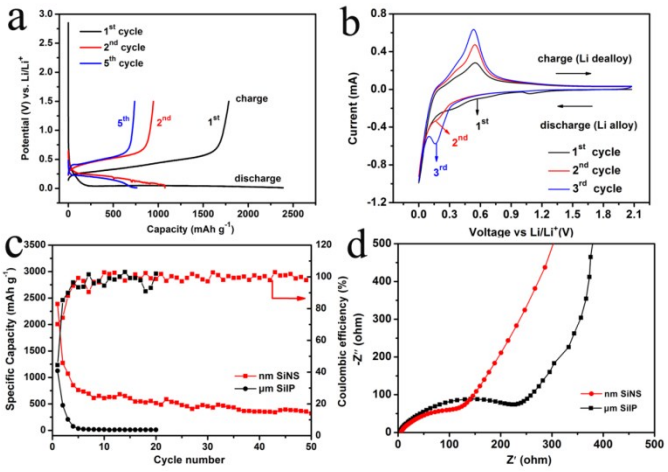

Fig. 6 The discharge and charge curves at a galvanostatic current density of 210 mA g^{-1} cycled between the voltage of 1.5–0.01 V vs Li/Li^+ (a), and CV curves at a scan rate of 0.1 mV s^{-1} in the cut off voltage of 1.5–0.01 V vs Li/Li^+ (b) of SiNS; Cycling performance at 210 mA g^{-1} (c), and electrochemical impedance spectra (d) of SiNS and μm SiIP electrodes before cycling.

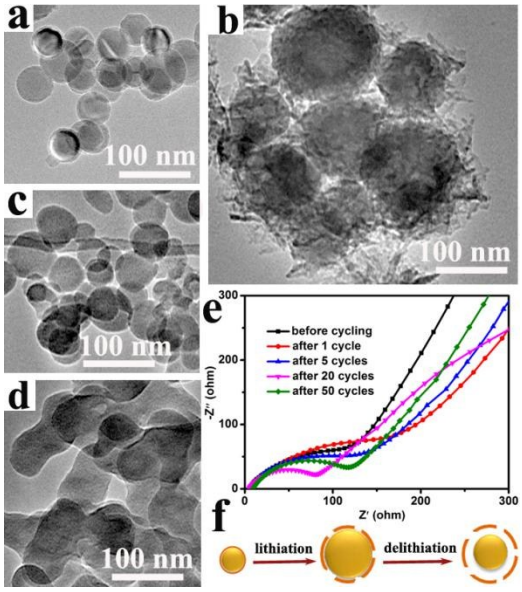

Fig. 7 SEM images of the SiNS anode before cycling (a), fully lithiated (b), after 1cycle (c), and after 20 cycles (d); electrochemical impedance spectra obtained after different cycles (e); and schematic of the SiNS electrode's lithiation–delithiation mechanism (f).

The improvement of the lithium storage properties could be fundamentally attributed to the microstructural stability of SiNS during cycling process. The microstructure changes of SiNS electrode during cycling process were confirmed by the TEM images as shown in Fig. 7. TEM images of the SiNS electrode before (Fig. 7a) and after (Fig. 7b) lithiation reveal that the SiNSs undergo obvious volume expansion as lithium inserts. The average diameter increases from ~50 to ~70 nm, corresponding to a 270% volume expansion. This result is far less than the volume change previously reported in literatures (400%), indicating that SiNSs could effectively reduce the volume changes during charge-discharging. Importantly, after lithium extraction process, the diameter of SiNS is recovered, and the spherical morphology is well maintained (Fig. 7c). After 20 cycles, as is shown in Fig. 7d, although the SiNSs have become coarser, the spherical morphology is basically maintained, and no obvious fracture is observed, indicating that the SiNS electrode could withstand volume expansion and remain stable for long cycles. The evolution of the electrochemical and physical properties of the electrodes during cycling process can also be inferred from EIS data.[64] Fig. 7e exhibits the impedance of SiNS electrode after different cycles. A decrease of the semicircle is observed between the first and the subsequent plots. But after the 50th cycle, the semicircle shows slight increase, indicating the impedance of SiNS electrode begins to slowly increase, which matches well with the microstructure change of SiNS electrode (Fig. 7c and d).

Although SiNS electrode shows great structural stability during cycling, the volume expansion during the initial lithium insertion process still could break the SEI layer (Fig. 7f), exposing new surface of Si to the electrolyte solvents. This further leads to the consuming of available electrolytes, corresponding to the irreversible capacity and lower ICE phenomenon in the initial cycle (Fig. 6c). Thus, constructing a buffer layer to isolate SiNSs from direct contact with the electrolytes is essential.

Fig. 8 shows the electrochemical performance of SiNS/PC composites with different Si/C ratios (SiNS/PC-0.5:1, SiNS/PC-1:1 and SiNS/PC-4:1), and the electrochemical performance of PC could be seen in Fig. S5. The specific capacity values of SiNS/PC composites were calculated on the basis of the total weight of SiNS and PC. Fig. 8a demonstrates the initial charge and discharge curves of all samples at a current density of 210 mA g^{-1}. Similar to that of SiNS (Fig. 6a), the initial cycle discharge-charge curves of SiNS/PC composites show a broader discharge lithiation voltage plateau at 0.05-0.1 V, and a charge delithiation voltage plateau at 0.35-0.45 V.[52-53] The discharge and charge capacities of SiNS/PC composites in the first cycle are about 1151 and 822.6 mA h g^{-1} for SiNS/PC-0.5:1, 1902.6 and 1216.2 mA h g^{-1} for SiNS/PC-1:1, and 2105.2 and 1730.1 mA h g^{-1} for SiNS/PC-4:1, with the ICE of 71.5, 64.0, and 82.2%, respectively. Compared to pure SiNS, the SiNS/PC composites show obviously improved initial coulombic efficiency (ICE), suggesting that the carbon shell effectively insulates the Si core from the electrolyte solvent and reduces the occurrence of side reactions of Si with electrolyte.[65] Cyclic voltammetry (CV) was further conducted to characterize the electrochemical performance of the SiNS/PC composite. As shown in Fig. 8b, the two peaks at 0.01 and 0.16 V at the cathodic branch (Li alloy) of the CV curve are corresponding to the formation of Li_xSi alloy phases, while the two peaks at 0.35 and 0.52 V at the anodic branch (Li dealloy) could be ascribed to de-lithiation back to Si.[66] Due to the contribution of carbon to the overall anode capacity, the peaks of SiNS/PC exhibit a little left shift originating from the C delithiation.[27]

The cycling performances of all SiNS/PC composites at the current density of 210 mA g^{-1} are shown in Fig. 8c. For SiNS/PC composites, the initial specific capacities are 1151, 1190 and 2510 mA h g^{-1}, respectively, which are lower than that of the SiNS because of the presence of the carbon shell. But the coulombic efficiencies of the composites increase quickly and

stabilize at 99.5% in later cycles. Importantly, all SiNS/PC electrodes show improved cycling performance than the pure SiNS electrode (Fig. 6c). Specially, even after 50 cycles, the specific discharge capacity of SiNS/PC-4:1 is still 1278.8 mA h g^{-1}, which is 3.5 times that of the theoretical capacity of graphite anode (372 mA h g^{-1}). The great capacity retention for the SiNS/PC composite electrodes could be attributed to the unique structure of the SiNS/PC composite. The Si core contribute to its high capacity,[67] and the carbon coating shell, which enhances the conductivity and works as buffer layer to suppress the volume changes during cycling, mainly contributing to its good cycling stability. The electrochemical impedance spectroscopy (EIS) of all SiNS/PC composites were also studied and shown in Fig. 8d. A decrease of the semicircle is observed with the increase of SiNS content in composites, but all SiNS/PC electrodes show larger resistance than that of pure SiNS and pure PC. It is ascribed to the increased interfacial charge-transfer resistance introduced by the interface between the SiNS core and the PC layer of SiNS/PC composites.

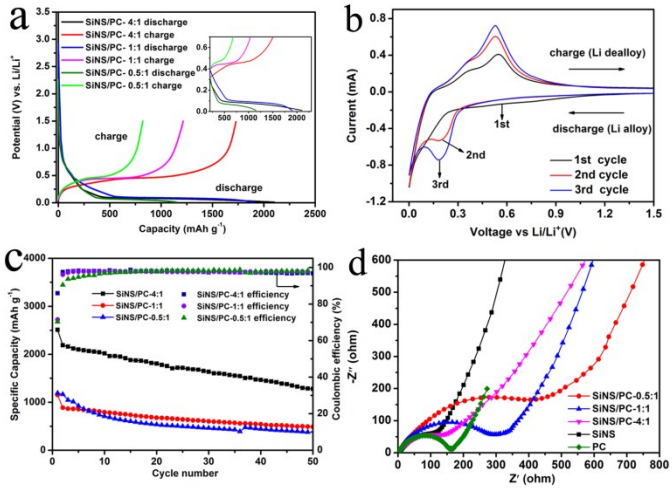

Fig. 8 (a) The initial discharge and charge curves of SiNS and SiNS/PC composites (SiNS/PC-0.5:1, SiNS/PC-1:1 and SiNS/PC-4:1) at a galvanostatic current density of 210 mA g^{-1} cycled between the voltage of 1.5–0.01 V vs Li/Li^+, (b) CV curves of SiNS/PC composite at a scan rate of 0.1 mV s^{-1} in the cut off voltage of 1.5–0.01 V vs Li/Li^+, (c) Cycling performance of SiNS and SiNS/PC composites (SiNS/PC-0.5:1, SiNS/PC-1:1 and SiNS/PC-4:1) electrode at 210 mA g^{-1}, (d) Electrochemical impedance spectra of SiNS, PC and SiNS/PC composites before cycling.

Due to the superior electrochemical performance of SiNS/PC-4:1 composite, the cycling performance and rate capability were further systematically investigated. As shown in Fig. 9a, the cycling performance curve of SiNS/PC-4:1 electrode exhibits stable plot with overall shape and shows slow descending tendency. Importantly, even after 100 cycles, the SiNS/PC-4:1 electrode still exhibits a high capacity of 778 mA h g^{-1} at the current density of 210 mA g^{-1}, corresponding to 2.1 times that of the theoretical capacity of graphite anode. Rate capability of anode materials is also very important especially for batteries applied in electric vehicles.[68] To systematically investigate the rate capability, the electrode was cycled at a current density of 420 mA g^{-1} for the initial 10 cycles. Then the current density was gradually increased to 840 mA g^{-1}, 2100 mA g^{-1}, 4200 mA g^{-1} and finally returned to 420 mA g^{-1} again. As shown in Fig. 9b, at the current density of 420 mA g^{-1}, the SiNS/PC-4:1 composite electrode shows a first discharge capacity of 2110 mA h g^{-1} with a coulombic efficiency of 82%. After two cycles, the reversible capacity stabilizes at 1965 mA h g^{-1} and the coulombic efficiency increases to 98.6%. At a higher current density of 840 mA g^{-1} and 2100 mA g^{-1}, the SiNS/PC-4:1 composite electrode exhibits an average reversible capacity of 1650 and 1010 mA h g^{-1}, respectively. Even at a higher current density of 4200 mA g^{-1}, the reversible capacity reaches up to 445 mA h g^{-1}, which is still higher than that of graphite (372 mA h g^{-1}). Importantly, when the current density is reduced back to 420 mA g^{-1}, the reversible capacity quickly raises to 1450 mA h g^{-1}, further suggesting that the SiNS/PC composite could remain stable even under extremely high current density.

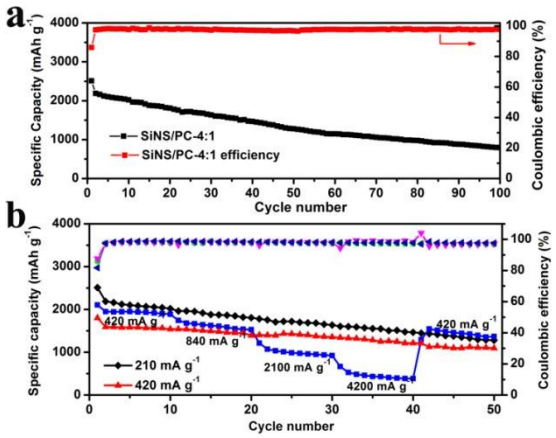

Fig. 9 (a) Cycling performance of SiNS/PC-4:1 composites electrode at 210 mA g^{-1} for 100 cycles, (b) Rate performance of the prepared SiNS/PC-4:1 nanocomposite electrode at various current densities of 420, 840, 2100 and 4200 mA g^{-1}.

The improvement of the lithium storage properties is believed to attribute to the microstructural stability of SiNS/PC composites during cycling process. The microstructural changes of SiNS/PC during cycling process were confirmed by the TEM images of the composite electrode before and after lithiation as shown in Fig. 10a-c. After 50 charge-discharge cycles, the SiNS/PC composites have underwent a little isotropic volume expansion, but most composite particles maintain the microstructure well and little fracture is observed in sight (Fig. 10b). Until after 100 charge-discharge cycles, the volume expansions of SiNS/PC composites become obvious and some particles become coarser. (Fig. 10c) In addition, the size distributions of the composite electrode before and after lithiation for 50 cycles were roughly measured and figured out by Nano-measurer program. As shown in Fig. 10d, the composites show a narrow size distribution of about 43 nm before lithiation and expand to 52 nm after 50 cycles, corresponding to a 174% volume expansion. The far less volume change of SiNS/PC composite could be attributed to the facts as follows: Firstly, the SiNS cores have much less volume changes during lithium insertion/extraction processes, which fundamentally alleviate the inner stress.[9] Secondly, the

porous carbon layer coated on the SiNS cores acts as constrained force to suppress the volume changes during cycling; Importantly, the micropores in the carbon shell could provide void space to accommodate the volume change. Furtherly, the microstructural stability of SiNS/PC composites ensure the stability of the solid electrolyte interphase (SEI) film, which is also a critical factor for obtaining long cycle life. As illustrated in Fig. 10e, for pure Si electrode, the large volume change during delithiation easily makes the SEI film broken. However, for SiNS/PC electrode, the unique structure of the composite could well accommodate the volume change and retain the SEI stability and thus lead to a good cycling performance.[69]

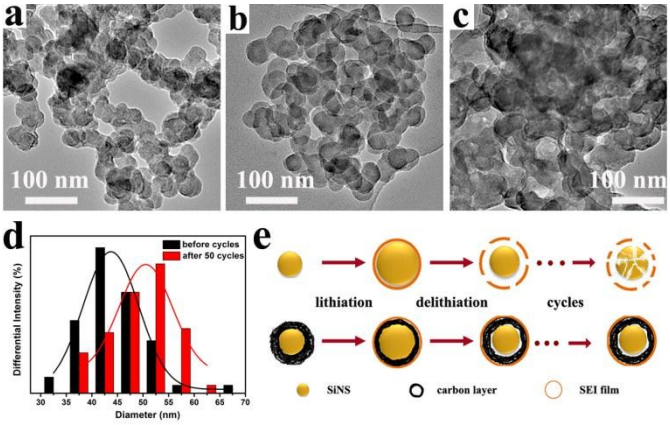

Fig. 10 TEM image of the SiNS/PC composite anode before cycle (a), after 50 cycles (b) and after 100 cycles (c); Particle size distribution of the SiNS/PC composite before cycle and after 50 cycles (d) and detailed schematic of the SiNS and SiNS/PC electrode's lithiation-delithiation mechanism (e).

4. Conclusions

In summary, large-scale Si nanospheres (SiNSs) have been synthesized via a simple, continuous and one-step way by using a radio frequency (RF) thermal plasma system. The as-obtained SiNSs display perfect spherical shape with smooth surface and good dispersity. As anode for LIBs, the SiNS electrode exhibits super electrochemical performance with an initial specific capacities of 2388 mA h g^{-1}. Even after 50 cycles, the specific discharge capacity of SiNS electrode is still 500 mA h g^{-1}. By a simple post-processing of ball-milling, SiNS/PC composites with Si nanospheres uniformly dispersed in the carbon matrix were synthesized. As anodes for LIBs, the obtained composite materials could maintain microstructural stability after cycles and exhibit remarkably improved electrochemical performance with large storage capacity, super cycling stability and high rate capability. Specially, the specific discharge capacity of SiNS/PC-4:1 could maintain at 1278.8 mA h g^{-1} even after 50 cycles at the current density of 210 mA g^{-1}, which is 3.5 times that of the theoretical capacity of graphite anode (372 mA h g^{-1}). More importantly, even after 100 cycles, the SiNS/PC-4:1 electrode still exhibits a high capacity of 778 mA h g^{-1}, corresponding to 2.1 times that of the theoretical capacity of graphite anode. Even at a higher current density of 4200 mA g^{-1}, the reversible capacity reaches up to 445 mA h g^{-1} and could quickly raise to 1450 mA h g^{-1} when the current density reduced back to 420 mA g^{-1}. These desirable electrochemical performances are attributed to the unique structure of the SiNS/PC composite: (1) The SiNS cores have high capacity and much less volume changes during lithium insertion/extraction processes, which fundamentally improve the capacity and alleviate the inner stress at the same time. (2) The porous carbon layer coated on the SiNS cores acts as constrained force to suppress the volume changes during cycling; (3) The micropores in the carbon shell provide void space to accommodate the volume changes; (4) Meanwhile, the carbon shell acts as a conductive matrix, which could enhance the conductivity and facilitate lithium-ion transportation during charge-discharge process. Importantly, the synthetic process of the unique structure can be readily scaled up, opening a viable way for practical applications of Si/C composites as anodes in future LIBs with high energy capacity.

Acknowledgements

The authors would like to acknowledge Bo Yan, a doctoral student at Institute of Process Engineering, CAS, for his contributions on the materials test.

Notes and references

1 J. Maier, *Nat. Mater*. 2005, **4**, 805.
2 M. Armand, J.-M. Tarascon, *Nature* 2008, **451**, 652.
3 X. Ji, K. T. Lee, L. F. Nazar, *Nat. Mater*. 2009, **8**, 500.
4 Y. G. Guo, J. S. Hu, L. J. Wan, *Adv. Mater*. 2008, **20**, 2878.
5 B. Xu, D. Qian, Z. Wang, Y. S. Meng, *Mater. Sci. Eng., R* 2012, **73**, 51.
6 M. Osiak, H. Geaney, E. Armstrong, C. O'Dwyer, *J. Mater. Chem. A* 2014, **2**, 9433.
7 Y. Yao, M. T. McDowell, I. Ryu, H. Wu, N. Liu, L. Hu, W. D. Nix, Y. Cui, *Nano Lett*. 2011, **11**, 2949.
8 X. Huang, J. Yang, S. Mao, J. Chang, P. B. Hallac, C. R. Fell, B. Metz, J. Jiang, P. T. Hurley, J. Chen, *Adv. Mater*. 2014, **25**, 4326.
9 H. Wu, Y. Cui, *Nano Today* 2012, **7**, 414.
10 X. Wang, H. Guan, S. Chen, H. Li, T. Zhai, D. Tang, Y. Bando, D. Golberg, *Chem. Commun.* 2011, **47**, 12280.
11 X. L. Huang, R. Z. Wang, D. Xu, Z. L. Wang, H. G. Wang, J. J. Xu, Z. Wu, Q. C. Liu, Y. Zhang, X. B. Zhang, *Adv. Funct. Mater*. 2013, **23**, 4345.
12 M.Zhou, Y. Liu, J. Chen, X. Yang, *J. Mater. Chem. A* 2015, **3**, 1068
13 X. Wang, X. Cao, L. Bourgeois, H. Guan, S. Chen, Y. Zhong, D. M. Tang, H. Li, T. Zhai, L. Li, *Adv. Funct. Mater*. 2012, **22**, 2682.
14 R. Hu, W. Sun, H. Liu, M. Zeng, M. Zhu, *Nanoscale*, 2013, **5**, 11971.
15 Z. Jian, B. Zhao, P. Liu, F. Li, M. Zheng, M. Chen, Y. Shi, H. Zhou, *Chem. Commun*. 2014, **50**, 1215.
16 J. Lin, A. R. O. Raji, K. Nan, Z. Peng, Z. Yan, E. L. Samuel, D. Natelson, J. M. Tour, *Adv. Funct. Mater.* 2014, **24**, 2044.
17 Z. Ju, C. Guo, Y. Qian, B. Tang, S. Xiong, *Nanoscale* 2014, **6**, 3268.

18 H. Liu, G. Wang, J. Liu, S. Qiao, H. Ahn, *J. Mater. Chem*. 2011, **21**, 3046
19 C. K. Chan, H. Peng, G. Liu, K. McIlwrath, X. F. Zhang, R. A. Huggins, Y. Cui, *Nature nanotechnology* 2007, **3**, 31.
20 H. Ma, F. Cheng, J. Y. Chen, J. Z. Zhao, C. S. Li, Z. L. Tao, J. Liang, *Adv. Mater*. 2007, **19**, 4067.
21 M. Ge, J. Rong, X. Fang, C. Zhou, *Nano Lett*. 2012, **12**, 2318.
22 H. Kim, M. Seo, M. H. Park, J. Cho, *Angew. Chem. Int. Ed*. 2010, **49**, 2146.
23 Y. Wang, Y. Wang, E. Hosono, K. Wang, H. Zhou, *Angew. Chem. Int. Ed*. 2008, **120**, 7571.
24 Y. Yu, L. Gu, C. Zhu, S. Tsukimoto, P. A. van Aken, J. Maier, *Adv. Mater*. 2010, **22**, 2247.
25 H. Li, X. Huang, L. Chen, Z. Wu, Y. Liang, Electrochem. *Solid-State Lett*. 1999, **2**, 547.
26 J.-M. Tarascon, M. Armand, *Nature* 2001, **414**, 359.
27 A. Magasinski, P. Dixon, B. Hertzberg, A. Kvit, J. Ayala, G. Yushin, *Nat. Mater*. 2010, **9**, 353.
28 M. R. Zamfir, H. T. Nguyen, E. Moyen, Y. H. Lee, D. Pribat, *J. Mater. Chem. A* 2013, **1**, 9566.
29 X. Li, Y. Xiao, J. H. Bang, D. Lausch, S. Meyer, P. T. Miclea, J. Y. Jung, S. L. Schweizer, J. H. Lee, R. B. Wehrspohn, *Adv. Mater*. 2013, **25**, 3187.
30 J. K. Yoo, J. Kim, Y. S. Jung, K. Kang, *Adv. Mater*. 2012, **24**, 5452.
31 L.-F. Cui, L. Hu, J. W. Choi, Y. Cui, *ACS Nano* 2010, **4**, 3671.
32 N. Liu, H. Wu, M. T. McDowell, Y. Yao, C. Wang, Y. Cui, *Nano Lett*. 2012, **12**, 3315.
33 L. Pan, H. Wang, D. Gao, S. Chen, L. Tan, L. Li, *Chem. Commun*. 2014, **50**, 5878.
34 R. Hu, W. Sun, Y. Chen, M. Zeng, M. Zhu, *J. Mater. Chem. A* 2014, **2**, 9118.
35 S.-L. Chou, J.-Z. Wang, M. Choucair, H.-K. Liu, J. A. Stride, S.-X. Dou, *Electrochem. Commun.* 2010, **12**, 303.
36 Y. Kwon, G.-S. Park, J. Cho, *Electrochim. Acta* 2007, **52**, 4663.
37 J.-H. Lee, W.-J. Kim, J.-Y. Kim, S.-H. Lim, S.-M. Lee, *J. Power Sources* 2008, **176**, 353.
38 W. Sun, R. Hu, H. Liu, M. Zeng, L. Yang, H. Wang, M. Zhu, *J. Power Sources*, 2014, **268**, 610.
39 K. A. Pettigrew, Q. Liu, P. P. Power, S. M. Kauzlarich, *Chem. Mater*. 2003, **15**, 4005
40 R. K. Baldwin, K. A. Pettigrew, J. C. Garno, P. P. Power, G.-y. Liu, S. M. Kauzlarich, *J. Am. Chem. Soc*. 2002, **124**, 1150.
41 K. Littau, P. Szajowski, A. Muller, A. Kortan, L. Brus, *J. Phys. Chem*. 1993, **97**, 1224.
42 X. Li, Y. He, M. T. Swihart, *Langmuir* 2004, **20**, 4720.
43 A. Onischuk, A. Levykin, V. Strunin, M. Ushakova, R. Samoilova, K. Sabelfeld, V. Panfilov, *J. Aerosol Sci* 2000, **31**, 879.
44 G. Hou, B. Cheng, F. Ding, M. Yao, P. Hu, F. Yuan, *ACS Appl. Mater. Interfaces* 2015, **7**, 2873.
45 O. Renault, R. Marlier, N. Barrett, E. Martinez, T. Baron, M. Gely, B. De Salvo, *Surf. Interface Anal*. 2006, **38**, 486.
46 M. N. Islam, T. Ghosh, K. Chopra, H. Acharya, *Thin Solid Films* 1996, **280**, 20.
47 S. Major, S. Kumar, M. Bhatnagar, K. Chopra, *Appl. Phys. Lett*. 1986, **49**, 394.
48 L. Yue, W. Zhang, J. Yang, L. Zhang, *Electrochim. Acta* 2014, **125**, 206.
49 B. B. Li, D. P. Yu, S. L. Zhang, *Phys. Rev. B* 1999, **59**, 1645.
50 L. Yin, J. Wang, F. Lin, J. Yang, Y. Nuli, *Energy Environ. Sci.* 2012, **5**, 6966.
51 J. C. Groen, L. A. A. Peffer, J. Perez-Ramirez, *Microporous Mesoporous Mater*. 2003, **60**, 1.
52 R. Hu, W. Sun, Y. Chen, M. Zeng, M. Zhu, *J. Mater. Chem. A* 2014, **2**, 9118.
53 J. Chang, X. Huang, G. Zhou, S. Cui, P. B. Hallac, J. Jiang, P. T. Hurley, J. Chen, *Adv. Mater*. 2014, **26**, 758.
54 J. Luo, X. Zhao, J. Wu, H. D. Jang, H. H. Kung, J. Huang, *J. Phys. Chem. Lett.* 2012, **3**, 1824.
55 B. Hertzberg, A. Alexeev, G. Yushin, *J. Am. Chem. Soc*. 2010, **132**, 8548.
56 B. Gao, S. Sinha, L. Fleming, O. Zhou, *Adv. Mater*. 2001, **13**, 816.
57 Y. S. Hu, R. Demir-Cakan, M. M. Titirici, J. O. Müller, R. Schlögl, M. Antonietti, J. Maier, *Angew. Chem. Int. Ed*. 2008, **47**, 1645.
58 V. Baranchugov, E. Markevich, E. Pollak, G. Salitra, D. Aurbach, *Electrochem. Commun*. 2007, **9**, 796.
59 R. A. Huggins, *J. Power Sources* 1999, **81**, 13.
60 J. Li, J. Dahn, *J. Electrochem. Soc*. 2007, **154**, A156.
61 Y. Ru, D. G. Evans, H. Zhu, W. Yang, *RSC Adv*. 2014, **4**, 71.
62 X.-y. Zhou, J.-j. Tang, J. Yang, J. Xie, L.-l. Ma, *Electrochim. Acta* 2013, **87**, 663.
63 X. Su, Q. Wu, J. Li, X. Xiao, A. Lott, W. Lu, B. W. Sheldon, J. Wu, *Adv. Energy Mater*. 2014, **4**,1.
64 J. Guo, A. Sun, X. Chen, C. Wang, A. Manivannan, *Electrochim. Acta* 2011, **56**, 3981.
65 H. Kim, B. Han, J. Choo, J. Cho, *Angew. Chem. Int. Ed*. 2008, **47**, 10151.
66 E. Pollak, G. Salitra, V. Baranchugov, D. Aurbach, *J. Phys. Chem. C* 2007, **111**, 11437.
67 X. Li, P. Meduri, X. Chen, W. Qi, M. H. Engelhard, W. Xu, F. Ding, J. Xiao, W. Wang, C. Wang, *J. Mater. Chem*. 2012, **22**, 11014.
68 H. Han, T. Song, E.-K. Lee, A. Devadoss, Y. Jeon, J. Ha, Y.-C. Chung, Y.-M. Choi, Y.-G. Jung, U. Paik, *ACS Nano* 2012, **6**, 8308.
69 C. Du, M. Chen, L. Wang, G. Yin, *J. Mater. Chem*. 2011, **21**, 15692.

Table of Contents

Highly dispersed Si nanospheres and Silicon nanosphere/porous-carbon composites with super electrochemical performance are successfully synthesized via thermal plasma and ball-milling.

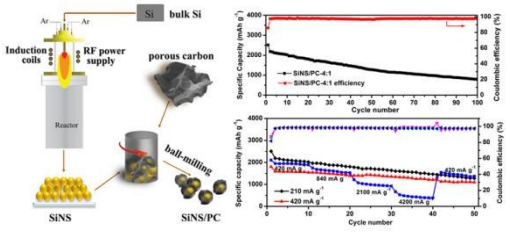

ToC Figure